Journal of the Meteorological Society of Japan, Vol. 87A, pp. 119–136, 2009
DOI:10.2151/jmsj.87A.119

GSMaP Passive Microwave Precipitation Retrieval Algorithm : Algorithm Description and Validation

Kazumasa AONASHI

Meteorological Research Institute, Tsukuba, Japan

Jun AWAKA

Department of Marine Biology and Sciences, Tokai University, Sapporo Campus, Sapporo, Japan

Masafumi HIROSE

Faculty of Science and Technology, Meijo University, Nagoya, Japan

Toshikaki KOZU

Interdisciplinary Faculty of Science and Engineering, Shimane University, Matsue, Japan

Takuji KUBOTA

Earth Observation Research Center, Japan Aerospace Exploration Agency, Tsukuba, Japan

Guosheng LIU

Department of Meteorology, Florida State University, Tallahassee, Florida, USA

Shoichi SHIGE, Satoshi KIDA

Department of Aerospace Engineering, Osaka Prefecture University, Sakai, Japan

Sinta SETO

Institute of Industrial Science, The University of Tokyo, Tokyo, Japan

Nobuhiro TAKAHASHI

National Institute of Information and Communications Technology, Koganei, Japan

and

Yukari N. TAKAYABU

Center for Climate System Research, The University of Tokyo, Kashiwa, Japan

(Manuscript received 29 June 2008, in final form 23 December 2008)

Corresponding author: Kazumasa Aonashi, Meteorological Research Institute, 1-1 Nagamine, Tsukuba, 305-0052, Japan
E-mail: aonashi@mri-jma.go.jp

Abstract

This paper describes a precipitation-retrieval algorithm for the Tropical Rainfall Measuring Mission (TRMM) Microwave Imager (TMI) that was developed under the Global Satellite Mapping of Precipitation project (GSMaP) by improving the authors' previous algorithm. The basic idea of the GSMaP algorithm is to find the optimal precipitation for which the brightness temperatures (TBs) calculated by the radiative-transfer model (RTM) fit best with the observed TBs. The main improvements of the GSMaP algorithm over the authors' previous work are as follows: (1) use of precipitation-related variable models (precipitation profiles, drop-size distribution, etc.) and precipitation detection and inhomogeneity estimation methods based on TRMM observation studies; (2) use of scattering signals of the TMI Polarization-Corrected Temperature (PCT) at 37 and 85 GHz (PCT37, PCT85) and scattering-signal correction for tall precipitation (thickness between precipitation top level and freezing level (Dtop) larger than 6 km) over land and coastal areas.

In order to validate the GSMaP algorithm, we compared its retrievals from TMI TBs in 1998 with the TRMM Precipitation Radar (PR) and Goddard Profiling Algorithm (GPROF) retrievals (2A12 version 6). The results show that (1) over land and coastal areas, the GSMaP retrievals agreed better with PR than GPROF for tall precipitation (Dtop > 4 km) weaker than 10 mm h^{-1}, while both GSMaP and GPROF underestimated PR precipitation rates for precipitation heavier than 10 mm h^{-1}; (2) over ocean, the GSMaP retrievals agreed better with PR than GPROF for precipitation heavier than 10 mm h^{-1}, while GSMaP slightly overestimated precipitation weaker than 10 mm h^{-1} compared to PR and GPROF; (3) The GSMaP algorithm failed to detect some precipitation areas weaker than 2 mm h^{-1} over sub-tropical oceans.

Experimental algorithms with different precipitation-related variable models and retrieval methods using scattering signals were applied to TMI TBs in July 1998 to examine the effect of the above improvements to the GSMaP algorithm. The results show that the improvement of the precipitation profile alleviated the underestimation of precipitation heavier than 10 mm h^{-1} over land and coastal areas, that the combined use of new physical-related variable models alleviated the underestimation of precipitation heavier than 10 mm h^{-1} over ocean, and that the use of PCT37 and scattering-signal correction reduced the overestimation of tall precipitation (Dtop > 4 km) weaker than 10 mm h^{-1} over land and coastal areas.

1. Introduction

Satellite passive microwave radiometer (MWR) brightness temperatures (TBs) give information on emission from raindrops and scattering by frozen particles. MWRs recently have become the principal sensors for global precipitation retrieval, since these emission and scattering signals (lower-frequency TB increases and higher-frequency TB depressions from a precipitation-free atmosphere) have a more direct relationship with precipitation rates than infrared radiometer (IR) cloud-top TBs (Ebert and Manton 1998).

MWR precipitation retrieval algorithms are generally classified as either statistical or physical. Statistical algorithms (e.g., Grody 1991; McCollum and Ferraro 2003) require observed precipitation data sets to derive the empirical relationship between precipitation rates and TBs. Physical algorithms (e.g., Panegrossi et al. 1998; Kummerow et al. 2001; Aonashi and Liu 2000) require a priori models for precipitation-related variables and radiative-transfer models (RTMs) in order to calculate look-up tables (LUTs) relating to precipitation rates and TBs.

Before the TRMM launch, global information on the precipitation-related variables was sparse. Accordingly, conventional statistical algorithms depended on observed precipitation data sets taken over limited areas. Conventional physical algorithms resorted to precipitation-related variable models based on a small number of field campaigns (Aonashi and Liu 2000, hereafter referred to as AL) or cloud-resolving model outputs (Panegrossi et al. 1998; Kummerow et al. 2001).

Recent studies using TRMM data, however, have revealed the global distribution of various precipitation-related variables, such as particle size and precipitation types (e.g., Kozu et al. 2009; Takayabu 2006). The TRMM data have also enabled us to research the statistical relationship between TBs and the precipitation-related variables (e.g., Seto et al. 2005; Kubota et

al. 2007, 2009; Kida et al. 2009).

Under the Global Satellite Mapping of Precipitation project (GSMaP), we developed a new physical precipitation retrieval algorithm (hereafter referred to as the GSMaP algorithm) by improving the AL algorithm based on the above studies. The main improvements in the GSMaP algorithm are as follows: (1) use of precipitation-related variable models and precipitation detection and inhomogeneity-estimation methods based on TRMM observation studies; (2) use of the scattering signals of Polarization-Corrected Temperature (PCT) at 37 and 85 GHz (PCT37, PCT85) and scattering-signal correction for tall precipitation over land and coastal areas.

The purpose of the present study is to describe the GSMaP algorithm and to report its validation results. To this end, we compared its retrievals from TRMM Microwave Imager (TMI) TBs in 1998 with the TRMM Precipitation Radar (PR) and the Goddard Profiling Algorithm (GPROF) retrievals. We also applied experimental algorithms with different precipitation-related variable models and retrieval methods, using scattering signals of TMI TBs in July 1998 to examine the effects of the above improvements in the GSMaP algorithm.

2. Data used in the present study

2.1 TMI

TMI is a five-frequency, nine-channel, conical-scanning MWR that measures at 10.7, 19.7, 21.3, 37, and 85.5 GHz (hereafter referred to as 10, 19, 21, 37, and 85 GHz) with an incident angle of 52.8 degrees. As seen in Table 1, each frequency has one vertically (V) and one horizontally (H) polarized channel, except for the water-vapor absorption band at 21 GHz, which has only a vertical polarization channel. Table 1 also gives beam effective Fields-Of-Views (FOVs) for each TMI channel. The swath width of TMI is limited to 760 km because of the low orbital altitude of TRMM (about 400 km).

Table 1. TMI Frequencies, Polarizations, and Beam effective FOVs.

Frequency (GHz)	Polarization	Beam effective FOVs (km)
10.65	V & H	63 x 37
19.35	V & H	30 x 18
21.3	V	23 x 18
37.0	V & H	16 x 9
85.5	V & H	7 x 5

In the present study, we used TMI 1B11 version 6 for the MWR TB data. The surface condition flags of the 1B11 TBs were classified into land, ocean, and coast, based on the land/ocean coverage within the 10 GHz FOVs.

2.2 PR

PR is a nadir-looking weather radar measuring back-scattered energy from precipitating particles at 13.8 GHz. The horizontal and vertical resolutions of PR are 4.3 km and 250 m. PR has a swath width of 215 km, though low-level echoes near swath boundaries are contaminated by ground clutter.

In the validation, we used PR 2A25 version 6 for the PR precipitation data. PR 2A25 includes precipitation profiles, rain flags for various kinds (convective, stratiform, bright band, etc.), and range bin numbers of various precipitation-related variables (top level, bright-band levels, etc.) (Iguchi 2007; Iguchi et al. 2009).

2.3 GPROF

In the validation, we used TMI 2A12 version 6 precipitation data, which is the output of GPROF (the current NASA operational rainfall algorithm). GPROF retrieves instantaneous rainfall using a Bayesian approach to match the observed TBs to those calculated from CRM variables. More information on the retrieval algorithm is available in Kummerow et al. (2001) and Olson et al. (2006).

3. Algorithm description

The basic idea of the GSMaP algorithm is to determine the precipitation rates that yield RTM-calculated TBs that best fit with TMI TBs, the same as that of AL. The GSMaP algorithm employs PCT37 and PCT85 over land and coast and TBs with vertical polarization at 10, 19, and 37 GHz (TB10v, TB19V, and TB37v), in addition to PCT37 and PCT85 over ocean. The GSMaP algorithm consists of a forward-calculation part to calculate the LUTs and a retrieval part to estimate precipitation rates from the observed TBs using the LUTs.

3.1 Forward calculation

As Fig. 1 schematically illustrates, the RTM calculation requires information on atmospheric variables

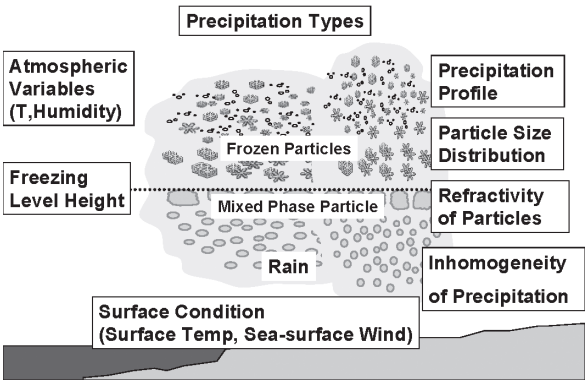

Fig. 1. Schematic illustration of information required for the RTM calculation.

(temperature, relative humidity, freezing level height (FLH), cloud liquid water content (CLWC), etc.), surface variables (surface temperature, sea-surface wind speed), and precipitation-related variables (precipitation profiles, precipitating-particle size distribution, refractivity of frozen and mixed-phased particles, horizontal inhomogeneity of precipitation, etc.).

This subsection will describe the above physical variables and the RTM calculation methods used in the GSMaP algorithm. (We will discuss the precipitation inhomogeneity in Section 3.2 since it was estimated from the observed TBs.) As described in the introduction, the main improvement in the forward calculation part over AL is the use of new precipitation-related variable models, as summarized in Table 2.

a. Atmospheric and surface variables

We adopted the atmospheric temperature, FLH, and surface temperature over land and coast from the Japan Meteorological Agency (JMA) Global ANALysis data (GANAL), since GANAL gives a priori, global information on these variables with certain accuracy. Similarly, we adopted the sea-surface temperature from the JMA merged satellite and in situ data on global daily sea-surface temperatures in the ocean (MGDSST). For relative humidity and CLWC, we assumed the same constant values, 100% and 0.5 kg m^{-2}, as AL.

The LUTs were calculated for every 5 x 5 degree point within the latitude-longitude coordinates, as we will describe in Section 3.1.c. Thus, we incorporated the above variables for the 5 x 5 degree points into the RTM calculation.

b. Precipitation-related variable models

We adopted the following convective and stratiform precipitation models for the precipitation-related variables:

(1) Precipitation profile

We constructed statistical precipitation profile models using TRMM observations. To this end, we first classified PR data into 10 types (six over land, four over ocean and coast) using the PR precipitation parameters (rain area, stratiform rain-area fraction, precipitation-top level, etc.) and the ratio between the PR precipitation rates and TRMM Lightning Imaging Sensor (LIS) flash rates (Takayabu 2006).

We then produced convective and stratiform precipitation profile models for these types by averaging the PR convective and stratiform precipitation profiles over prescribed precipitation ranges for each type. In this averaging, we used profiles relative to FLH in order to exclude the influence of atmospheric temperature variations (Kubota et al. 2007).

Table 2. Main differences in precipitation-related variable models of the AL and GSMaP algorithms.

Precipitation-related variables	AL	GSMaP
Precipitation profile	Constant vertical gradients	The PR profiles averaged for each precipitation types
Raindrop size distribution	Marshall-Palmer distribution	Kozu et al. (2008) model
Mixed-phase particle size distribution and refractivity	Neglected	Nishitsuji et al. (1983) model for stratiform precipitation

(2) Precipitating-particle size distribution models

For the raindrop-size distribution, we constructed statistical models for each precipitation type using globally available PR observations (Kozu et al. 2009). To this end, we first assumed a gamma distribution for the raindrop size:

$$N(D) = N_0 D^{\mu} \exp(-\lambda D), \quad (1)$$

where N is the number concentration for particles with diameter D, μ=3, and N_0 and λ are parameters to be determined. For convective precipitation, we calibrated N_0 and λ using attenuation-corrected factors derived from the PR data. For stratiform precipitation, we used the standard values for N_0 and λ of PR 2A25 version 6. We then averaged the above values for each precipitation type to produce statistical models of raindrop-size distribution.

Conventional models were used for frozen and mixed-phase particle-size distributions that could not be estimated from the TRMM observations. For the frozen-particle size distribution, we applied the Marshall Palmer distribution to both convective and stratiform precipitation, similar to AL. The particle-size distribution for mixed-phase stratiform precipitation (between FLH minus 1 km and FLH) was parameterized in terms of atmospheric temperature (Nishituji et al. 1983). We neglected mixed-phase convective precipitation.

(3) Refractivity of frozen and mixed-phase particles

We calculated the refractivity of convective and stratiform frozen particles, assuming them to be a mixture of ice and air with an empirically prescribed constant density (200 kg m^{-3}), similar to AL. The refractivity of mixed-phase stratiform particles was parameterized in terms of atmospheric temperature (Nishituji et al. 1983).

c. RTM calculation methods

First, we calculated the convective and stratiform LUTs for horizontally homogeneous precipitation by incorporating the above atmospheric-, surface-, and precipitation-related variables into the RTM program of Liu (1998). This program computed TBs for a plane-parallel atmosphere using a four-stream approximation. In this program, all precipitation particles were assumed to be spherical, and the absorption and scattering coefficients and the phase functions were computed based on the Mie theory.

We then derived convective and stratiform LUTs with various horizontal precipitation inhomogeneities using the approximation of AL. This approximation converted TBs for homogeneous precipitation (TB^h) into those for inhomogeneous precipitation (TB^i), assuming a lognormal distribution of the precipitation:

$$TB^i = \int \frac{1}{\sqrt{2\pi\xi}} \exp\left[-\frac{1}{2\xi^2}(\ln(pr) - \overline{\ln(pr)})^2\right] TB^h \, d\ln(pr), \quad (2)$$

where $\ln(pr)$ is the natural logarithm of the precipitation, and $\overline{\ln(pr)}$ and ξ are the average and the standard deviation of $\ln(pr)$.

The LUTs used in the retrieval part were weighted averages of the above convective and stratiform LUTs. The weights were determined by the statistical frequency distribution of the PR convective and stratiform precipitation for each precipitation type and surface precipitation rate.

3.2 Retrieval part

This subsection will describe the procedures of the retrieval part, schematically illustrated in Fig. 2. As described in the introduction, the main improvements in the retrieval part over AL are as follows: (1) new precipitation detection and inhomogeneity estimation

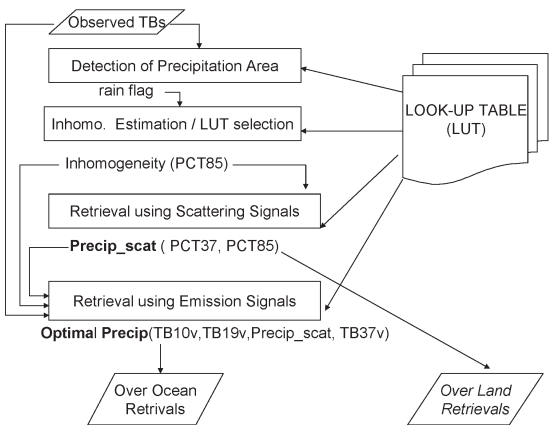

Fig. 2. Schematic illustration of procedures in the retrieval part of the GSMaP algorithm.

methods based on TRMM observation studies; (2) a new scattering retrieval method using PCT37 and PCT85 and scattering-signal correction for tall precipitation.

a. Detection of precipitating areas

Over land, we adopted the detection methods of Seto et al. (2005). We calculated the scattering indices from TMI TB85v and TB21v, and judged that precipitating areas had scattering indices larger than the statistically determined thresholds. Since this method mistook snow cover for precipitation, we regarded all areas with surface temperatures lower than 273.2 K as precipitation-free.

Over coastal areas, we used the method of Kubota et al. (2007). This is an improvement of McCollum and Ferraro (2005) that detects precipitating areas using PCT85 scattering signals and a decision tree of several empirical conditions for TMI TBs.

Over ocean, we adopted the method of Kida et al. (2009). We judged that precipitating areas had either PCT85 scattering or TB37v emission signals, which were expressed by the respective TMI PCT85 depressions and TB37v increases from the LUT TBs for 0 mm h^{-1}.

b. Estimation of precipitation inhomogeneity

We used high-resolution PCT85 to estimate the standard deviation of the natural logarithm of the precipitation (SDNLPR), similar to AL.

First, we converted the PCT85 scattering signals into precipitation (Rain85) using LUTs for a prescribed value of SDNLPR (=1.0), and calculated a first guess of the inhomogeneity (Sigma85) from Rain85 within the TB10v FOVs.

This first guess was then adjusted based on the statistical relationship between Sigma85 and SDNLPR calculated from PR (Kubota et al. 2009). The LUTs for this adjusted value were used in the following retrieval procedures.

c. Precipitation retrieval using scattering signals

As scattering signals for precipitation retrieval, we chose PCT37 in addition to PCT85, in spite of the coarser resolution and smaller signals of PCT37. This was based on the following comparison results between the TMI scattering signals and the thickness between the PR precipitation top levels and FLH (Dtop). Figure 3 illustrates the relationship between Dtop and the scattering-signal ratios of the TMI observations to the RTM calculation from the PR precipitation, over land, for July 2004. This indicates that the TMI PCT85 scattering signals were much more sensitive to Dtop than the RTM-calculated PCT85 scattering signals, and that the TMI PCT37 scattering signals were practically independent of Dtop, except

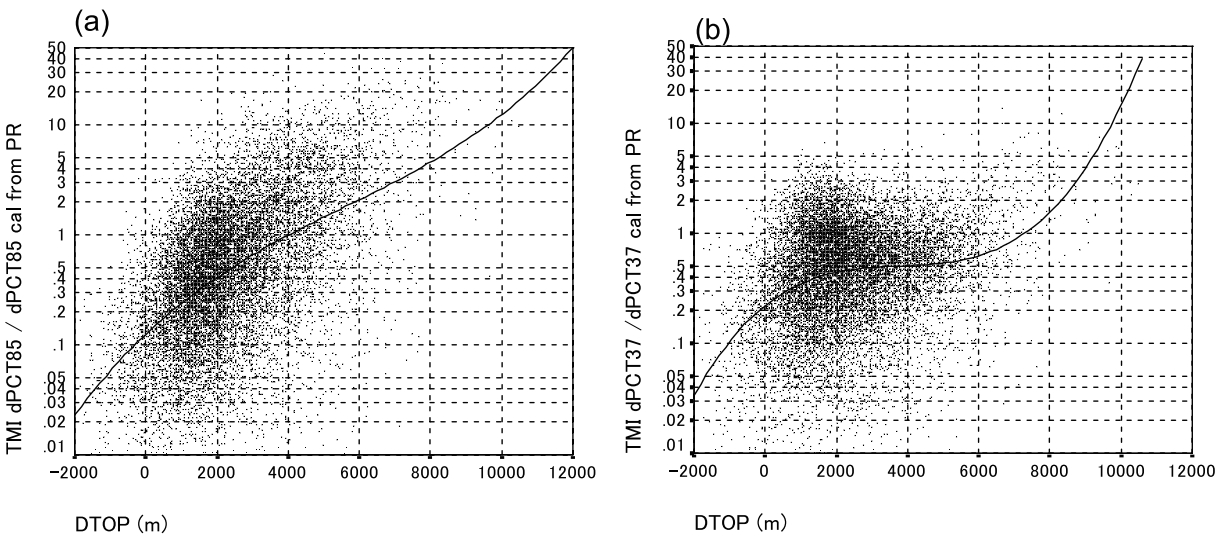

Fig. 3. Scatter diagram between Dtop (in m) and the scattering-signal ratios of the TMI observations to the RTM calculation based on the PR precipitation for (a) PCT85 and (b) PCT37 over land, for July 2004.

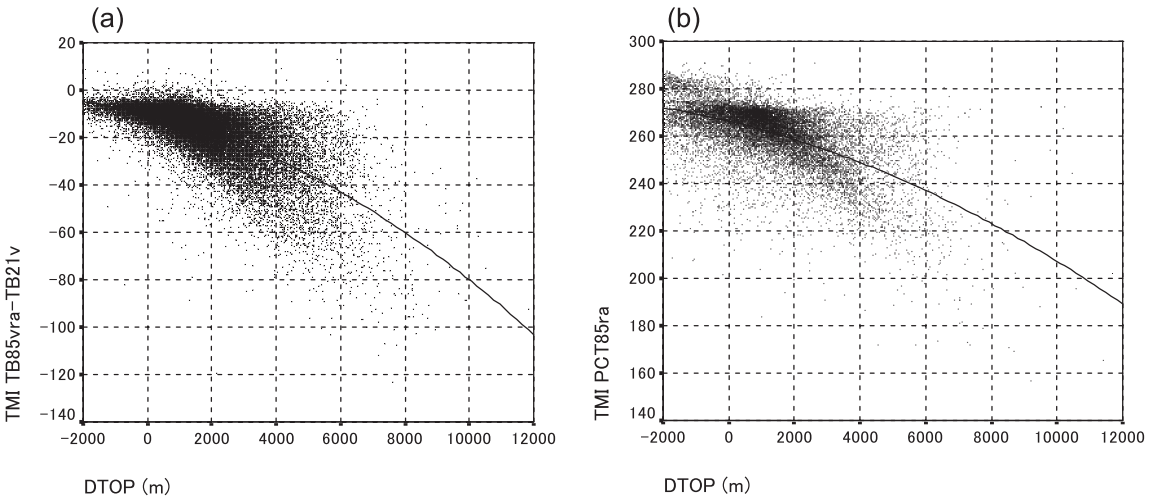

Fig. 4. Scatter diagram between (a) Dtop (in m) and TB85v minus TB21v (in K) in precipitating areas over land and (b) Dtop and PCT85 (in K) in precipitating areas over coast, for July 2004.

for tall precipitation (Dtop > 6 km).

Based on the above results, we combined the PCT85 and PCT37 scattering signals for the retrieval as follows.

(1) The LUTs for PCT37 were statistically corrected for tall precipitation over land and coast.

(2) Rain85 was adjusted by precipitation retrieved from PCT37 (Rain37).

The LUT correction for tall precipitation required Dtop estimation using TMI TBs. Over land (coast), we employed TB85v minus TB21v (PCT85) in precipitating areas as the indices of Dtop (see Fig. 4) and statistically estimated Dtop from these variables.

We derived the statistical ratios of the TMI PCT37 scattering signals to those calculated from the PR surface precipitation and their dependency on Dtop, as seen in Fig. 3. We then corrected the LUTs for PCT37, using these statistical values for the TMI-estimated tall precipitation over land and coast.

Next, we retrieved Rain37 from the PCT37 scattering signals using the corrected LUTs. We adjusted Rain85 based on Rain37, multiplying Rain85 by 10 GHz-FOV averages of the ratio of Rain37 to Rain85. We output these adjusted values as precipitation retrievals using scattering signals (scattering retrieval), comprising the outputs of the GSMaP algorithm over land and coast.

d. Precipitation retrieval using emission signals over ocean

For retrieval over ocean, emission signals at lower frequencies were available in addition to the scattering signals. Similar to AL, the GSMaP algorithm found the optimal precipitation over ocean by minimizing a cost function (J) that was a weighted sum of squares of the differences between the observation and the forward calculation for TB10v and TB19v:

$$J = \sum_{f} \sum_{k=1}^{km} \frac{1}{2\sigma^2{}_f} \left\{ TB_f^0(\hat{y}_k) - TB_f^i\left[\hat{y}_k : r(\hat{x}_j)\right] \right\}^2, \qquad (3)$$

where $r(\hat{x}_j)$ is the precipitation at point $\hat{x}_j$, $\hat{y}_k$ is the location of a TMI pixel, TB_f^0 and TB_f^i represent the TMI TBs and the FOV-averaged TBs calculated from $r(\hat{x}_j)$ at frequency f. σ_f is the standard deviation of the differences between TB_f^0 and TB_f^i. Here $\sum_f$ represents summation for f=10 and 19 GHz, and $\sum_{k=1}^{km}$ is the summation of TMI pixels over ocean.

We derived the first guess for this minimization by adjusting the scattering retrievals based on precipitation retrieved from TB10v (Rain10v). In this adjustment, we multiplied the scattering retrievals by the 10 GHz-FOV averages of the ratio of scattering retrievals to Rain10v. For shallow precipitation with zero precipitation retrievals, we employed precipitation retrieved from TB37v (Rain37v) as the first guess.

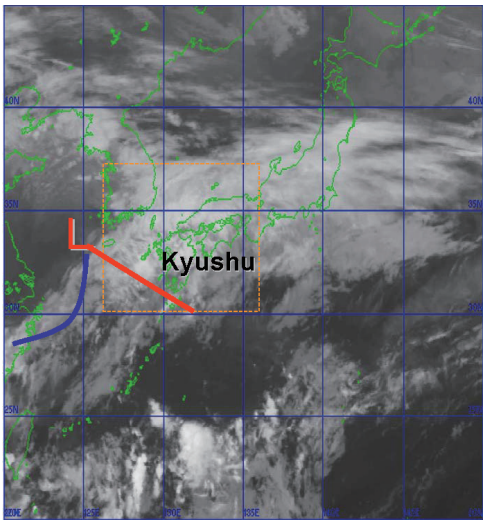

Fig. 5. GMS5 IR TB image for 18 UTC, June 1, 1998.

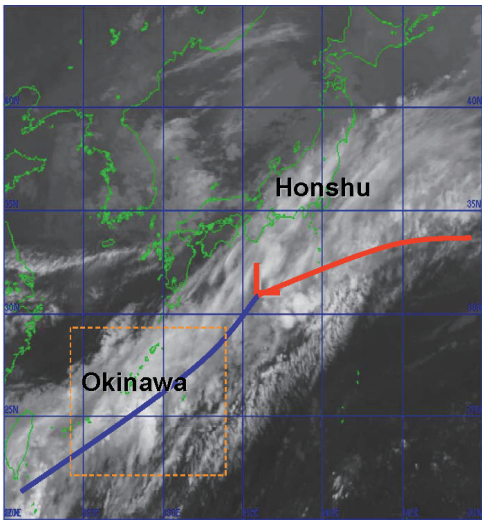

Fig. 7. GMS5 IR TB image for 15 UTC, June 5, 1998.

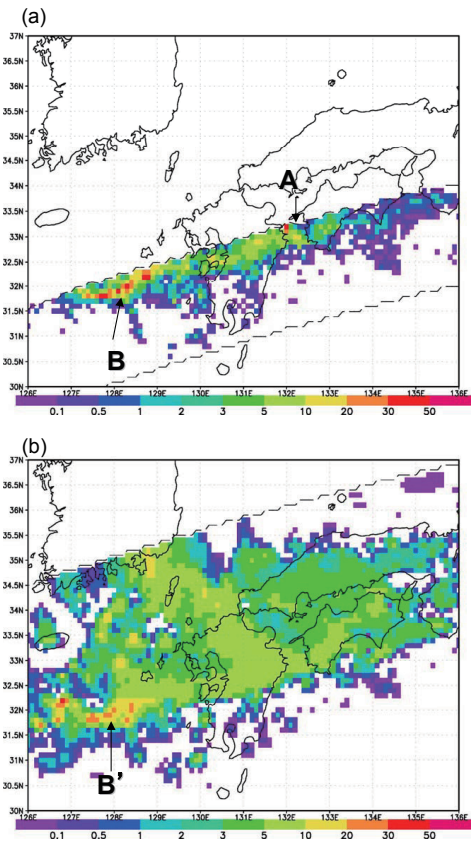

Fig. 6. Surface precipitation rates (in mm h^{-1}) for June 1, 1998.
(a) PR for OP 2931 (18 UTC).
(b) GSMaP precipitation retrievals for OP 2931 (18 UTC).

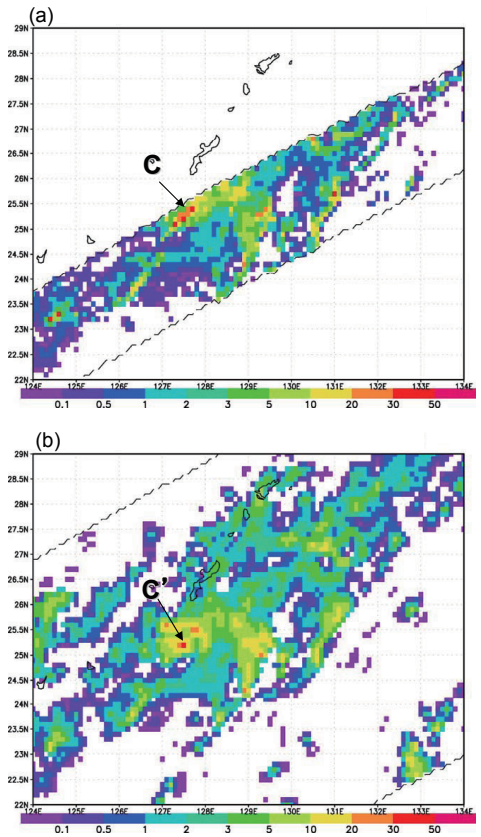

Fig. 8. Surface precipitation rates (in mm h^{-1}) for June 5, 1998.
(a) PR for OP 2992 (15 UTC).
(b) GSMaP precipitation retrievals for OP 2992 (15 UTC).

We obtained the optimal precipitation over ocean by AL's method of solving the gradient equation of the cost function.

4. Algorithm validation

We applied the GSMaP algorithm to TMI TBs for some Baiu (Japanese rainy season) cases in 1998. We also used the GSMaP algorithm for retrieving TMI global precipitation distributions for January, April, July, and October 1998. We then validated these precipitation retrievals using the PR precipitation rates. We also compared the GSMaP and GPROF global precipitation retrievals (2A12 version 6) for July 1998.

4.1 Baiu cases

In order to examine both over-land and over-ocean retrievals, we chose a precipitation case around Kyushu Island and a Baiu disturbance case near Okinawa.

a. Precipitation around Kyushu (18 UTC, June 1, 1998)

Figure 5 is a Japanese Geostationary Meteorological Satellite 5 (GMS5) IR TB image for 18 UTC on June 1. At this time, an extra-tropical low with fronts was moving eastward over the East China Sea. Most of Japan was covered with low-TB clouds, and precipitation was observed over a wide region of western Japan.

Figure 6 presents the PR surface precipitation rates and TMI precipitation rates retrieved with the GSMaP algorithm for TRMM Over-Path (OP) 2931 (~18 UTC) within the dashed-line box in Fig. 5. This indicates that, over land and coast, many precipitation retrievals fell into a range of 3 to 10 mm h^{-1}, and that heavier precipitation (at Point A, for example) was not retrieved by the GSMaP algorithm. Accordingly, the GSMaP algorithm overestimated (underestimated) PR surface precipitation weaker than 3 mm h^{-1} (heavier than 10 mm h^{-1}) over land and coast.

Over ocean, the GSMaP algorithm retrieved precipitation heavier than 10 mm h^{-1} (Points B and B'), while we found small-scale positional errors between the PR and the retrieved precipitation in heavy-precipitation areas.

b. Baiu disturbance near Okinawa (15 UTC, June 5, 1998)

Figure 7 is a GMS5 IR TB image taken at 15 UTC on June 5. At this time, the Baiu front extended over the sea from around Okinawa to south of Honshu Island. Low-TB clouds covered a wide region along the front, and meso-scale convective clouds were scattered around Okinawa.

Figure 8 presents the PR surface precipitation rates and TMI precipitation rates retrieved with the GSMaP algorithm for OP2992 (~15 UTC) within the dashed-line box in Fig. 7. Large-scale patterns in the precipitation retrievals agreed well with those measured by PR over ocean. Though we did find small-scale positional errors between the PR and the retrieved precipitation in heavy-precipitation areas (at Points C and C', for example). The GSMaP algorithm underestimated the maximum values of heavy precipitation over ocean, while it tended to overestimate the precipitation rates for the surrounding areas.

4.2 Global precipitation distributions for January, April, July, and October, 1998

We calculated the 10 GHz-FOV average of the instantaneous values of the GSMaP retrievals and the PR surface precipitation rates for January, April, July, and October 1998. In this calculation, we employed PR data around the swath centers (width 100 km) to avoid ground-clutter contamination. We then classified these averaged values using surface condition flags for the 10 GHz FOVs in order to examine the GSMaP algorithm's performance over land, coast, and ocean.

Figure 9 presents scatter diagrams of the over-land GSMaP retrievals and PR surface precipitation rates for the four months. The correlation coefficients between the over-land retrievals and PR were 0.6923 to 0.7677, with the correlation degrading for precipitation heavier than 10 mm h^{-1}. The scattering patterns varied little among the four months. On average, the over-land retrievals underestimated the PR precipitation, particularly in the heavy precipitation range (> 10 mm h^{-1}).

Figure 10 presents scatter diagrams of the over-coast GSMaP retrievals and the PR surface precipitation rates for the four months. The over-coast retrievals had error characteristics (underestimation of heavy precipitation) similar to the over-land retrievals. Though the correlation between the retrievals and PR over coast (0.6233 to 0.7075) was slightly worse than that over land. We think that this is mainly due to estimation error in the surface emission over coastal FOVs, which are a mixture of ocean and land areas.

Figure 11 presents scatter diagrams of the over-ocean GSMaP retrievals and PR surface precipitation rates for the four months. The over-ocean retrievals

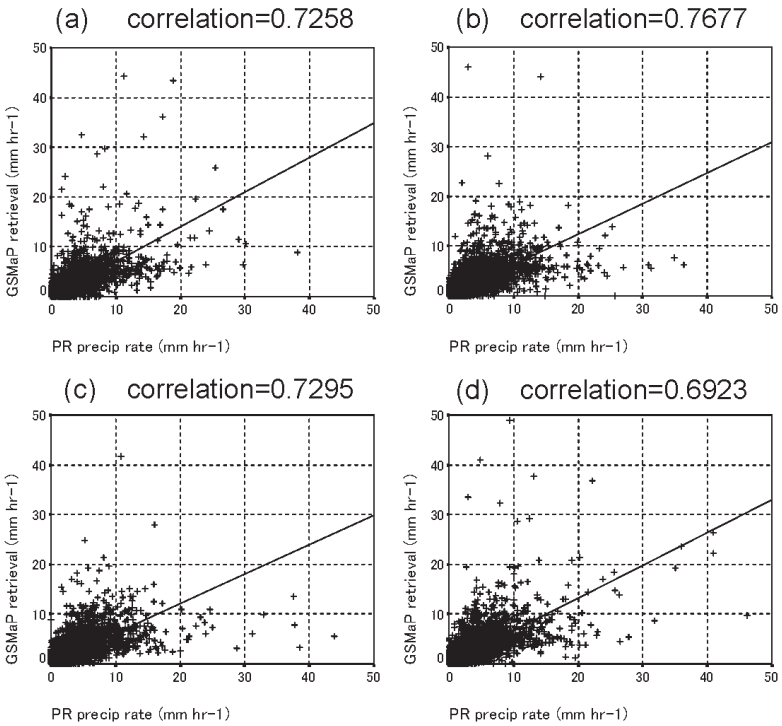

Fig. 9. Scatter diagrams of the over-land GSMaP precipitation retrievals and PR surface precipitation rates (in mm h^{-1}) for (a) January, (b) April, (c) July, and (d) October 1998.

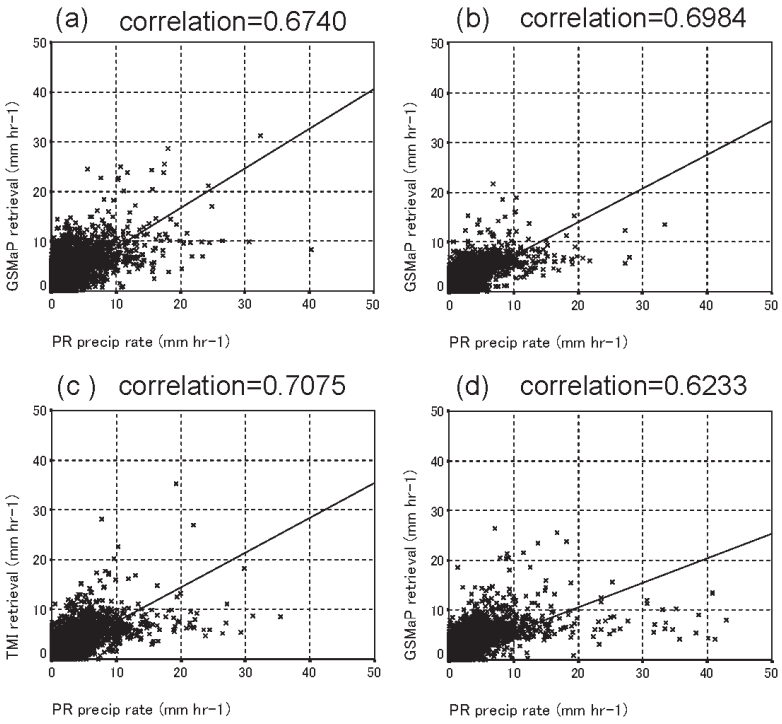

Fig. 10. The same as Fig. 9, but for over-coast GSMaP precipitation retrievals.

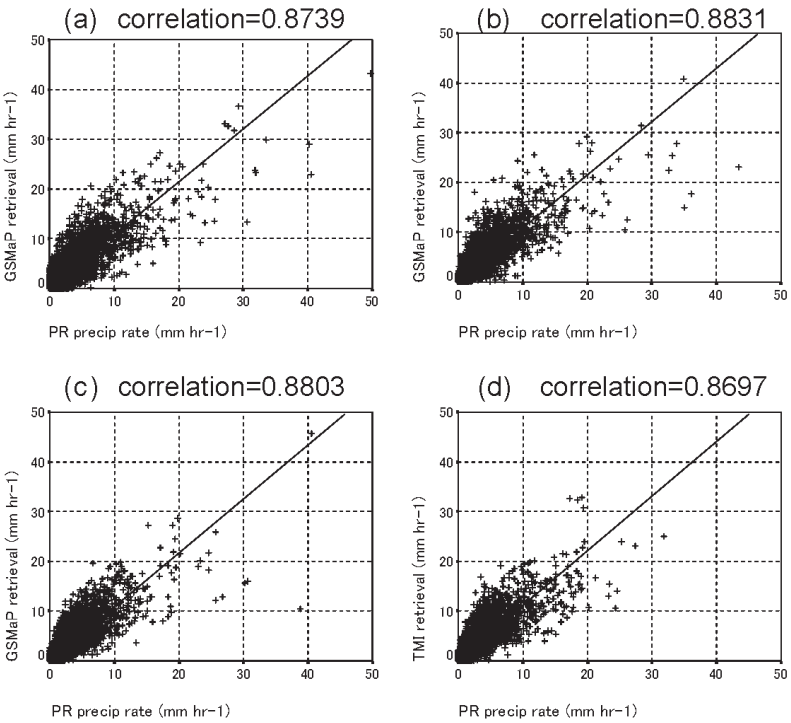

Fig. 11. The same as Fig. 9, but for over-ocean GSMaP precipitation retrievals.

agreed well with PR precipitation, as indicated by the higher correlation (0.8697 to 0.8831). It should also be noted that the scattering patterns varied little among the four months. However, we found a slight overestimation of PR precipitation weaker than 10 mm h^{-1}.

Next, we checked global maps of the monthly-mean precipitation rates of the GSMaP algorithm and their anomalies from PR (Figs. 12 and 13) in order to see the regional variations in the precipitation retrieval errors. The result suggests that the GSMaP algorithm tended to overestimate heavy-precipitation areas along the inter-tropical and sub-tropical convergence zones and the mid-latitude storm tracks, while it failed to detect some precipitation areas weaker than 2 mm h^{-1} over sub-tropical oceans. In contrast, we did not find systematic biases over land, except for mountainous regions like the southern slopes of the Himalayas, where orography-induced shallow convection was predominant.

4.3 Comparison with GPROF for July 1998

We calculated the 10 GHz-FOV average of the instantaneous values of the GPROF retrievals for July 1998, using the procedures described in Section 4.2.

Figure 14a (b) is a scatter diagram of the over-land GPROF (GSMaP) retrievals and PR surface precipitation rates for this month. Each point is classified in terms of Dtop. While GPROF overestimated tall precipitation (Dtop > 4 km) weaker than 10 mm h^{-1}, the GSMaP retrievals agreed better with PR than GPROF for this range. Since GPROF used only 85 GHz TBs as scattering signals, we think that this overestimation was caused by their sensitivity to tall precipitation. Both GSMaP and GPROF underestimated the PR precipitation rates for precipitation heavier than 10 mm h^{-1}, while GSMaP had larger retrieval errors for this range. We also found that over-coast retrievals had error characteristics similar to the over-land retrievals (Figure not shown).

Figure 14c (d) presents a Dtop-classified scatter diagram of the over-ocean GPROF (GSMaP) retrievals and PR surface precipitation rates for July 1998. While GPROF underestimated precipitation heavier than 10 mm h^{-1}, the GSMaP retrievals agreed better with PR than GPROF for this range. In contrast, the GPROF retrievals corresponded slightly better with PR precipitation rates than did the GSMaP retrievals for precipitation weaker than 10 mm h^{-1}. These error

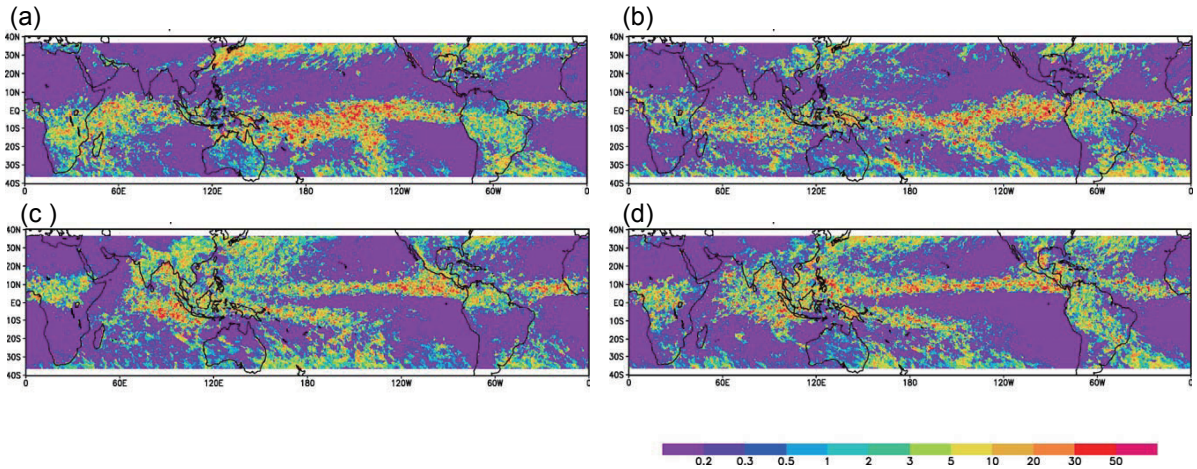

Fig. 12. Global maps of the monthly mean precipitation rates (in mm h^{-1}) in the GSMaP retrievals for (a) January, (b) April, (c) July, and (d) October 1998.

characteristics did not depend on Dtop, in contrast to the over-land scattering retrievals. Thus, we infer that they were caused by variable-model differences between the two algorithms related to the emission signals (e.g., rain profile, drop-size distribution, mixed-phase refractivity, etc.). The effects of these variable-model differences on GSMaP retrievals will be discussed in Section 5.1.

5. Retrieval experiments

As described in Section 3, the main improvements in the GSMaP algorithm over AL are: (1) new precipitation-related variable models; (2) new precipitation-detection and inhomogeneity-estimation methods; (3) a new scattering-retrieval method using PCT37 and PCT85 and scattering-signal correction for tall precipitation. In this section, we focus on the effects of the precipitation-related variable models and the scattering-retrieval method on the precipitation retrievals. (Precipitation-detection and inhomogeneity estima-

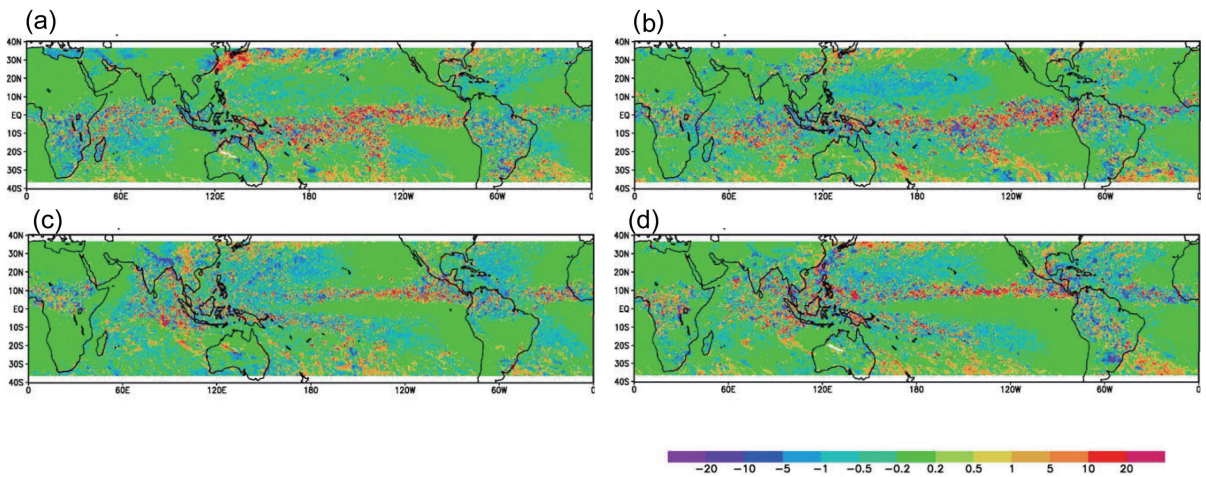

Fig. 13. Global maps of monthly mean precipitation-rate anomalies (in mm h^{-1}) between the GSMaP retrievals and PR for (a) January, (b) April, (c) July, and (d) October 1998.

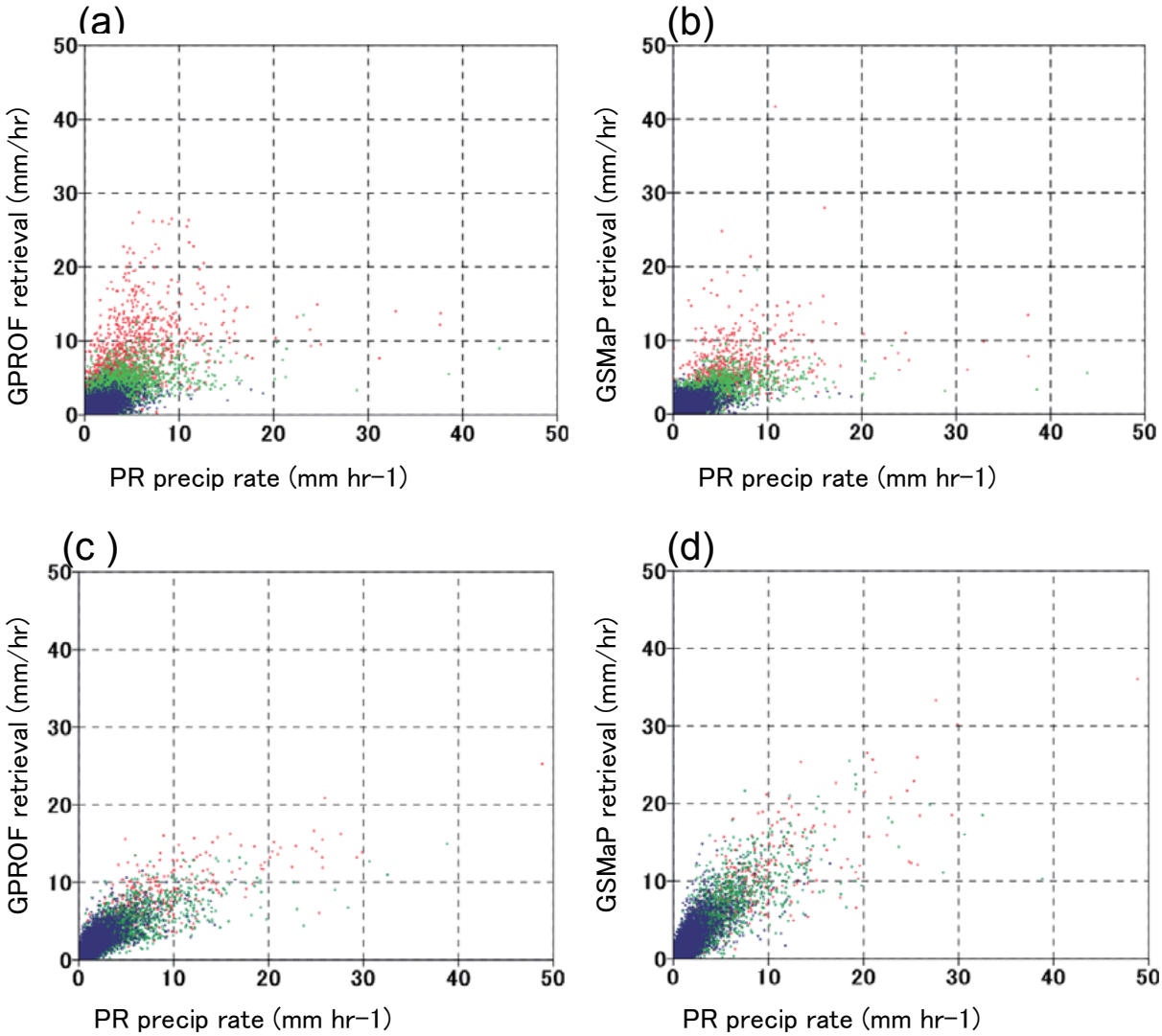

Fig. 14. Scatter diagrams of the retrievals and PR surface precipitation rates (in mm h^{-1}) for July 1998 for (a) GPROF over land, (b) GSMaP over land, (c) GPROF over ocean, and (d) GSMaP over ocean. Red, green, and blue dots are points with respective Dtop > 4 km, 2-4 km, and < 2 km.

tion methods have already been reported by Seto et al. 2005; Kubota et al. 2007, 2009; and Kida et al. 2009.)

To evaluate these effects, we developed experimental algorithms by switching off some of the above improvements. We applied these algorithms to TMI TBs for July 1998, and compared the outputs with the corresponding GSMaP retrievals.

5.1 Experiments on the precipitation-related variable models

For this purpose, we developed an experimental algorithm (EXP1) that used the AL models for all of the variables in Table 2 (other procedures were the same as GSMaP).

Figure 15a is a scatter diagram of the over-land EXP1 retrievals and PR surface precipitation rates for July 1998. Comparing this with Fig. 9c, we found that EXP1 exhibits a more severe underestimation of PR precipitation heavier than 5 mm h^{-1}. This means that the new precipitation-related variable models alleviated this underestimation. We also checked the over-land retrieval increments between GSMaP and EXP1

for this month. The results indicated significant differences in the increments, depending on the precipitation type (Section 3.1.b). For example (Fig. 15b), we had large positive increments for type 5, where organized medium top-level precipitation was dominant, while the increments were small for type 1 (tall thunderstorms).

Figure 15c is a scatter diagram of the over-ocean EXP1 retrievals and PR surface precipitation rates for this month. Comparing this with Fig. 11c, we found that EXP1 underestimated PR-measured precipitation heavier than 10 mm h^{-1} and that the new precipitation-related variable models alleviated this underestimation. We also found that the (GSMaP – EXP1) increments were large over the tropical ocean, compared to the mid-latitudes of the winter hemisphere (< 25 S), as

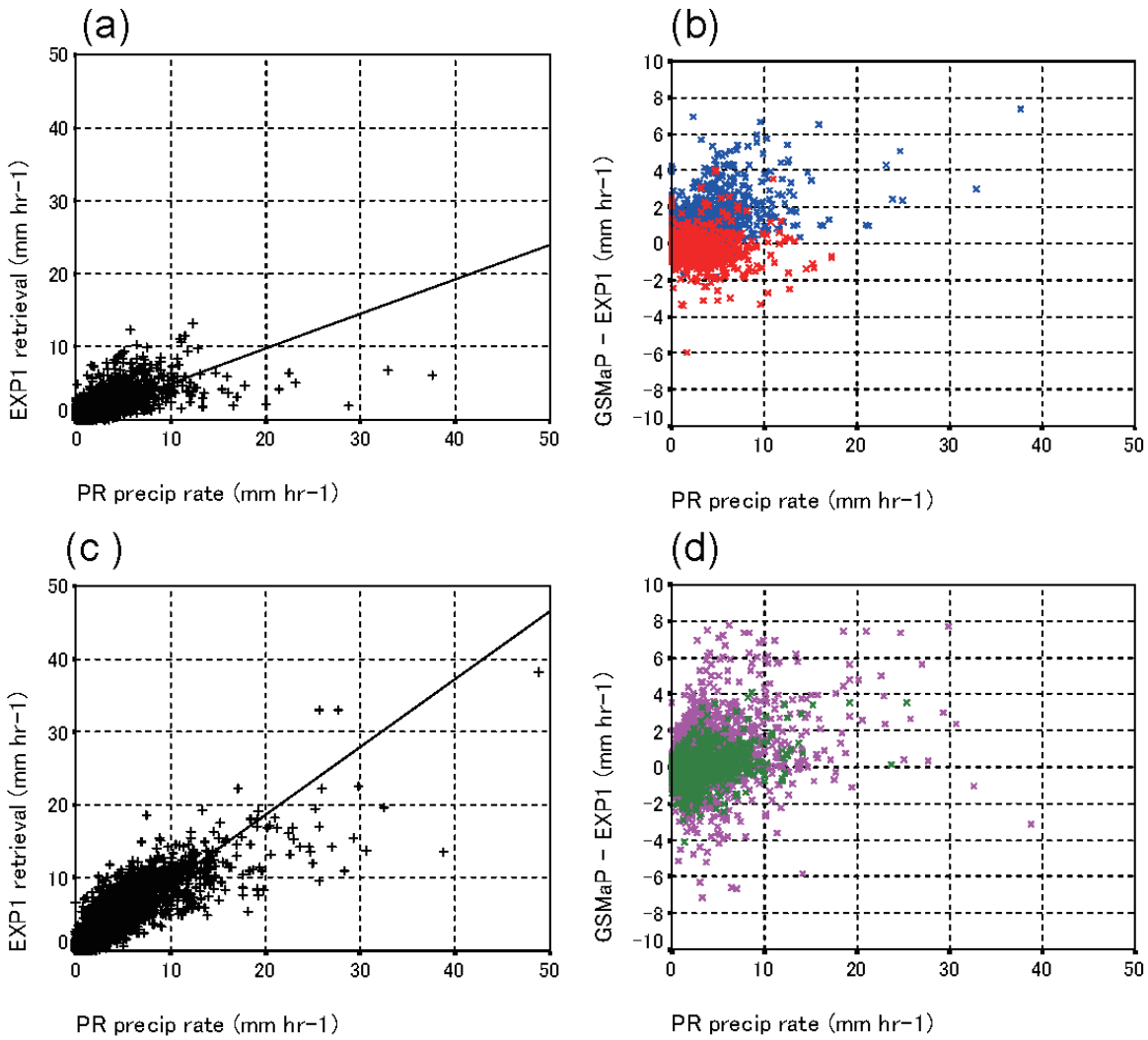

Fig. 15.
(a) Same as Fig. 9c, but for the EXP1 retrievals.
(b) Over-land precipitation retrieval differences (GSMaP minus EXP1) for July 1998. Red and blue are for precipitation types 1 and 5.
(c) Same as Fig. 11c, but for the EXP1 retrievals.
(d) Over-ocean precipitation retrieval differences (GSMaP minus EXP1) for July 1998. Pink and green are for the tropical and winter-hemisphere mid-latitudes (< 25 S).

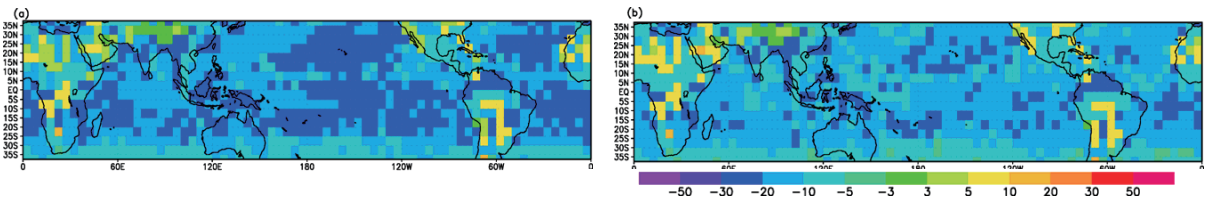

Fig. 16. PCT85 scattering-signal differences (in K) between GSMaP and the experiments for homogenous precipitation of 10 mm h^{-1} at 00 UTC, July 1, 1998 for (a) GSMaP minus EXP1 and (b) GSMaP minus EXP2.

seen in Fig. 15d.

We created further experimental algorithms that changed only the precipitation profile (EXP2), the raindrop-size distribution (EXP3), or the mixed-phase refractivity (EXP4) from the AL model in order to check the effect of each variable model. We then compared the forward-calculated TBs of EXP1-4 and GSMaP for 00 UTC on July 1, 1998.

Figure 16a (b) illustrates the differences between GSMaP and EXP1 (EXP2) in the calculated PCT85 scattering signals for homogeneous precipitation of 10 mm h^{-1}. The differences between GSMaP and EXP3,4 were negligible (Figure not shown). This means that the new precipitation-profile model played a dominant role in improving over-land and –coast GSMaP retrievals through its forward calculation of the scattering signals.

Figure 17 presents the differences between GSMaP and EXP1-4 in the calculated TB10v emission signals for the same case as in Fig. 16. This indicates that each of the three variable-model improvements significantly impacted the calculation of the emission signals, as opposed to the scattering signals. The new models for precipitation profiles and raindrop size distribution reduced the calculated emission signals except in the winter hemisphere mid-latitudes, where emission from rain became small because of low FLH. In contrast, the new mixed-phase model raised the calculated emission signals, in particular over the winter hemisphere mid-latitudes, where emission from mixed-phase precipitation became dominant. We consider that the combined effect of these new variable models provided more realistic LUTs that improve over-ocean GSMaP retrievals, particularly for heavy precipitation.

5.2 Experiments on scattering retrieval

For this purpose, we developed an experimental algorithm (EXP5) that used only PCT85 as the scattering signals, and we switched off the scattering-signal correction for tall precipitation (other procedures were the same as GSMaP). We also created an experimen-

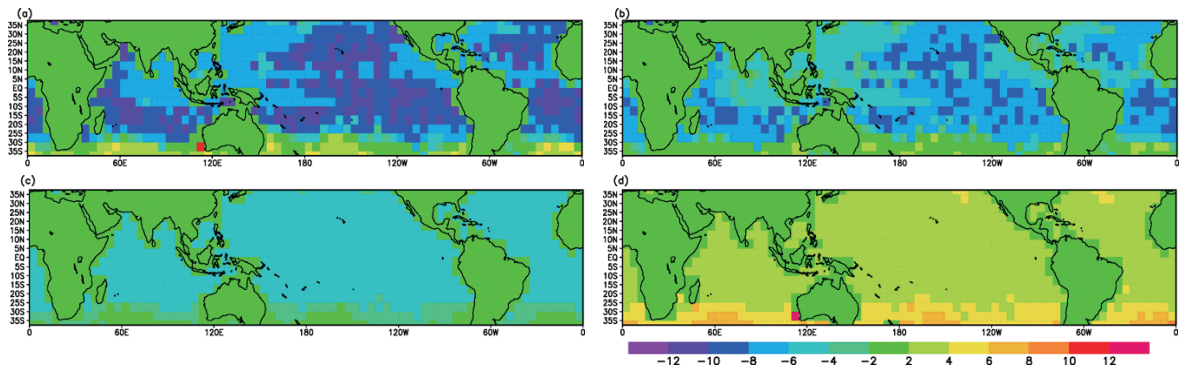

Fig. 17. TB10v emission-signal differences (in K) between GSMaP and the experiments for homogenous precipitation of 10 mm h^{-1} at 00 UTC, July 1, 1998.
(a) GSMaP minus EXP1; (b) GSMaP minus EXP2; (c) GSMaP minus EXP3; (d) GSMaP minus EXP4.

tal algorithm (EXP6) that only switched off the scattering-signal correction for tall precipitation.

Figure 18a (b) is a Dtop-classified scatter diagram of the over-land EXP5 (EXP6) retrievals and PR surface precipitation rates for July 1998. EXP5 extremely overestimated tall precipitation (Dtop > 4 km) weaker than 10 mm h^{-1}. EXP6 gave better retrievals than EXP5 by generally reducing the precipitation rates, though EXP6 still overestimated tall precipitation.

Comparing this with Fig. 14b, we found that the improvement in the scattering retrieval greatly alleviated the overestimation of tall precipitation (Dtop > 4 km) and enhanced the correspondence with PR over land. While the use of PCT37 contributed to this alleviation, it also exacerbated the underestimation of precipitation heavier than 10 mm h^{-1}. At the same time, the scattering-signal correction of tall precipitation was essential in diminishing the extreme overestimation.

6. Summary and discussion

This paper described a GSMaP passive microwave precipitation-retrieval algorithm developed by improving the AL algorithm. The main improvements in the GSMaP algorithm over AL are as follows: (1) use of precipitation-related variable models and precipitation detection and inhomogeneity estimation methods based on TRMM observation studies; (2) use of scattering signals of PCT37 and PCT85 and scattering-signal correction of tall precipitation over land and coast.

We validated the GSMaP retrievals using PR and GPROF data for 1998. The results are as follows:
(1) Over land and coast, the GSMaP retrievals agreed better with PR than GPROF for tall precipitation (Dtop > 4 km) weaker than 10 mm h^{-1}, while both GSMaP and GPROF underestimated PR precipitation rates for precipitation heavier than 10 mm h^{-1}.
(2) Over ocean, the GSMaP retrievals agreed better with PR than GPROF for precipitation heavier than 10 mm h^{-1}, while GSMaP slightly overestimated precipitation weaker than 10 mm h^{-1} compared with PR and GPROF .
(3) The GSMaP algorithm failed to detect some precipitation areas weaker than 2 mm h^{-1} over sub-tropical oceans.

The retrieval experiment results indicate that the improvement in the precipitation profile alleviated the underestimation of precipitation heavier than 10 mm h^{-1} over land and coast, that the combined use of new physical-related variable models alleviated the underestimation of precipitation heavier than 10 mm h^{-1} over ocean, and that the use of PCT37 and scattering-signal correction reduced the overestimation of tall precipitation (Dtop > 4 km) weaker than 10 mm h^{-1} over land and coast.

The validation and retrieval experiment results,

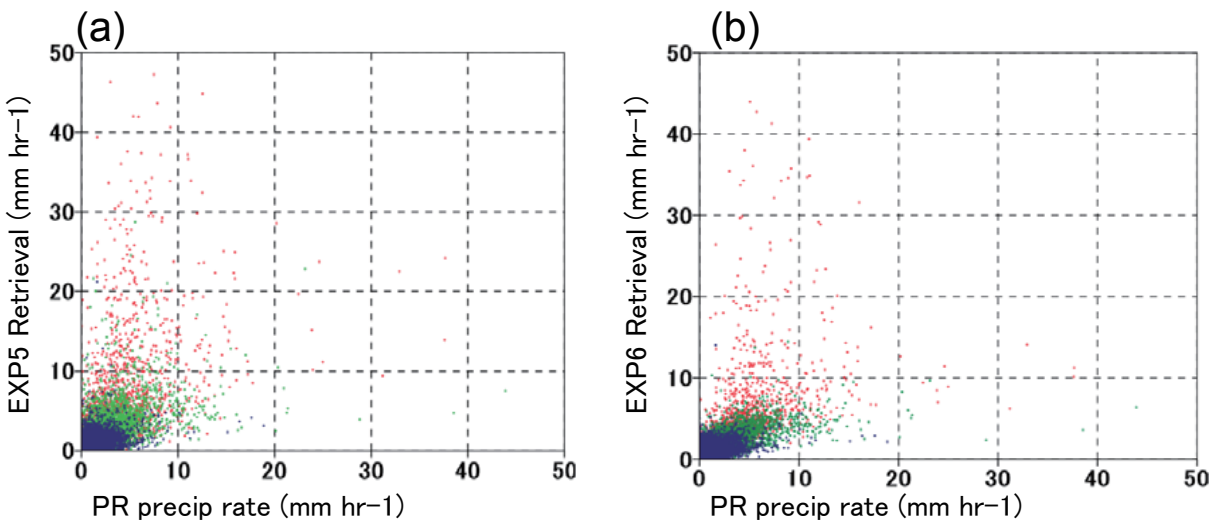

Fig. 18. Scatter diagrams of the retrievals and PR surface precipitation rates (in mm h^{-1}) during July 1998 for (a) EXP5 over land and (b) EXP6 over land. Red, green, and blue dots are points with respective Dtop > 4 km, 2-4 km, < 2 km.

however, indicate that the GSMaP algorithm had a problem in identifying heavy precipitation areas over land and coast, and underestimated precipitation heavier than 10 mm h^{-1}. This is mainly because the forward calculation exaggerated the PCT37 scattering signals for this precipitation range, compared to the TMI observation. Thus, solution of this problem requires improvement in the precipitation-related variable models and RTM program related to high-frequency scattering signals. We will work on the following points to achieve this improvement: (1) the introduction of the scattering effects of non-spherical frozen particles into the RTM program; (2) the search for a frozen-particle size distribution and density that gives LUTs close to the statistical relationship between the TMI scattering signals and PR precipitation rates.

The validation and retrieval experiment results over ocean suggest that the GSMaP algorithm chose the appropriate precipitation-related variable models in terms of the emission signals. Although the results also suggest a slight overestimation of weak precipitation surrounding heavy precipitation areas. One possible cause of this is that the low-frequency TBs in the surrounding areas became larger than those of the plane-parallel RTM calculation, since TMI observes TBs along slant paths (Kummerow et al. 2004). Hence, the overestimation could be due to the neglect of the 'slant-path effect' in the forward calculation. However, there is a possibility that PR underestimated the weak precipitation, as Shige et al. (2006, 2008) has pointed out. Accordingly, we will carefully examine the causes of this problem in an effort to reduce the overestimation.

We also found a detection problem over sub-tropical oceans where shallow precipitation is predominant. Kida et al. (2009) pointed out that the over-ocean precipitation-detection method of the GSMaP algorithm is less accurate than GPROF over these areas, and that the detection problem arose from the empirically determined, global assumptions concerning relative humidity (100%) and CLWC (0.5 kg m^{-2}) in the forward calculation. In order to improve the over-ocean precipitation detection method, we need to locate shallow precipitation regions and provide more realistic humidity and CLWC for these regions.

Acknowledgements

The present study was supported by "Production of a High-Precision, High-Resolution Global Precipitation Map Using Satellite Data" (the GSMaP project) under the "Core Research for Evolutional Science and Technology" program of the Japan Science and Technology Agency. The authors thank all team members of the GSMaP project, in particular Drs. Ken'ichi Okamoto, Tottori University of Environmental Studies, and Toshio Iguchi, National Institute of Information and Communications Technology. The GANAL and MGDSST data were provided by the Numerical Prediction Division of JMA.

References

Aonashi, K., and G. Liu, 2000: Passive microwave precipitation retrievals using TMI during the Baiu period of 1998. Part 1: Algorithm description and validation. *J. Appl. Meteor.*, **39**, 2024–2037.

Ebert, E. E., and M. J. Manton, 1998: Performance of satellite rainfall estimation algorithms during TOGA COARE. *J. Atmos. Sci.*, **55**, 1537–1557.

Grody, N., 1991: Classification of snow cover and precipitation using the special sensor microwave imager, *J. Geophys. Res.*, **96**(D4), 7423–7435.

Iguchi, T., 2007: *Space-borne radar algorithms in Measuring precipitation from space-EURAINSAT and the future*, V. Levizzani, P. Bauer, and F. J. Turk, Eds., Springer, 199–212.

Iguchi, T., T. Kozu, J. Kwiatkowski, R. Meneghini, J. Awaka, and K. Okamoto, 2009: Uncertainties in the rain profiling algorithm for the TRMM Precipitation Radar. *J. Meteor. Soc. Japan*, **87A**, 1–30.

Kida, S., S. Shige, T. Kubota, K. Aonashi, and K. Okamoto, 2009: Improvement of rain/no-rain classification methods for microwave radiometer observations over the ocean using a 37 GHz emission signature. *J. Meteor. Soc. Japan*, **87A**, 165–181.

Kozu, T., T. Iguchi, T. Kubota, N. Yoshida, S. Seto, J. Kwiatkowski, and Y. N. Takayabu, 2009: Feasibility of raindrop size distribution parameter estimation with TRMM Precipitation Radar. *J. Meteor. Soc. Japan*, **87A**, 53–66.

Kubota, T., S. Shige, H. Hashizume, K. Aonashi, N. Takahashi, S. Seto, M. Hirose, Y. N. Takayabu, K. Nakagawa, K. Iwanami, T. Ushio, M. Kachi, and K. Okamoto, 2007: Global precipitation map using satelliteborne microwave radiometers by the GSMaP project : Production and validation. *Trans. Geosci. Remote Sens.*, **45**, 7, 2259–

2275.

Kubota, T., S. Shige, K. Aonashi, and K. Okamoto, 2009: Development of nonuniform beamfilling correction method in rainfall retrievals for passive microwave radiometers over ocean using TRMM observations. *J. Meteor. Soc. Japan*, **87A**, 153–164.

Kummerow, C., Y. Hong, W. S. Olson, S. Yang, R. F. Adler, J. McCollum, R. Ferraro, G. Petty, D. B. Shin, and T. T. Wilheit, 2001: The Evolution of the Goddard Profiling Algorithm (GPROF) for rainfall estimation from passive microwave sensors. *J. Appl. Meteor.*, **40**, 1801–1820.

Kummerow, C., P. Poyner, W. Berg, and J. Thomas-Stahle, 2004: The effects of rainfall inhomogeneity on climate variability of rainfall estimated from passive microwave sensors. *J. Atmos. Oceanic Technol.*, **21**, 624–638.

Liu, G., 1998: A fast and accurate model for microwave radiance calculation. *J. Meteor. Soc. Japan*, **76**, 335–343.

McCollum, J. R., and R. R. Ferraro, 2003: Next generation of NOAA/NESDIS TMI, SSM/I, and AMSR-E microwave land rainfall algorithms. *J. Geophys. Res.*, **108**(D8), 8382, doi:10.1029/2001JD001512.

McCollum, J. R., and R. R. Ferraro, 2005: Microwave rainfall estimation along coasts. *J. Atmos. Ocean. Technol.*, **22**, 497–512.

Nishitsuji, A., M. Hoshiyama, J. Awaka, and Y. Furuhama, 1983: An analysis of propagative character at 34.5 GHz and 11.5 GHz between ETS-II satellite and Kasima station –On the precipitation model from stratus. *IEICE Trans.*, **Vol. J66-B**, 1163–1170, (in Japanese).

Olson, W. S., C. D. Kummerow, S. Yang, G. W. Petty, W.-K. Tao, T. L. Bell, S. A. Braun, Y. Wang, S. E. Lang, D. E. Johnson, and C. Chiu, 2006: Precipitation and latent heating distributions from satellite passive microwave radiometry. Part I: Improved method and uncertainties. *J. Appl. Meteor. Climatol.*, **45**, 702–720.

Panegrossi, G., S. Dietrich, F. S. Marzano, A. Mugnai, E. A. Smith, X. Xiang, G. J. Tripoli, P. K. Wang, and J. P. V. Poiares Baptista, 1998: Use of cloud model microphysics for passive microwave-based precipitation retrieval: Significance of consistency between model and measurement manifolds. *J. Atmos. Sci.*, **55**, 1644–1673.

Seto, S., N. Takahashi, and T. Iguchi, 2005: Rain/no-rain classification methods for microwave radiometer observations over land using statistical information for brightness temperatures under no-rain conditions. *J. Appl. Meteor.,* **44**. 1243–1259.

Shige, S., H. Sasaki, K. Okamoto, and T. Iguchi, 2006: Validation of rainfall estimates from the TRMM Precipitation Radar and microwave imager using a radiative transfer model: 1. Comparison of the version-5 and -6 products. *Geophys. Res. Lett.*, **33**, L13803, doi:10.1029/2006GL026350.

Shige, S., T. Watanabe, H. Sasaki, T. Kubota, S. Kida, and K. Okamoto, 2008: Validation of western and eastern Pacific rainfall estimates from the TRMM PR using a radiative transfer model. *J. Geophys. Res.*, **113**, D15116, doi:10.1029/2007JD009002.

Takayabu, N. Y., 2006: Rain-yield per flash calculated from TRMM PR and LIS data and its relationship to the contribution of tall convective rain. *Geophys. Res. Lett.*, **33**, L18705, doi:10.1029/2006GL027531.